applied sciences

MDPI

*Article*

# Facile Synthesis of $Ni^{3+}/Co^{3+}$ Ion-Doped $Zn_2SnO_4$ Microspheres toward Efficient Photocatalytic $CO_2$ Reduction

**Yanlong Yu [1], Jun Zhang [1], Yi Lin [1], Dandan Zhao [2], Ziying Li [3] and Sai Yan [1,*]**

[1] Faculty of Mathematics and Physics, Huaiyin Institute of Technology, Huaian 223003, China
[2] School of Science, Tianjin University of Commerce, Tianjin 300134, China
[3] School of Materials Science and Engineering, Nankai University, Tianjin 300350, China
* Correspondence: yansai@hyit.edu.cn

**Abstract:** The photocatalytic reduction of $CO_2$ into hydrocarbons is a promising solution for the energy crisis and greenhouse gas emissions. Thus, the fabrication and development of a new type of photocatalyst is of great importance for the practical application of $CO_2$ reduction. Herein, we report a facile synthesis of $Zn_2SnO_4$ (ZTO) microspheres doped with $Co^{3+}$ ions or $Ni^{3+}$ ions. The doped $Co^{3+}/Ni^{3+}$ ions substitute the lattice Zn/Sn ions. DFT calculations and experimental results reveal that the doped $Co^{3+}/Ni^{3+}$ ions would induce new doping energy levels in the band gap, extend the light response from the UV to the visible region, and separate the charge carriers. As a result, compared with pure ZTO, the photocatalytic activity of a $CO_2$ reduction into $CH_4$ is significantly improved for Co-doped ZTO (Co-ZTO) and Ni-doped ZTO (Ni-ZTO).

**Keywords:** $CO_2$ reduction; Co-doped ZTO; Ni doped ZTO; photocatalysis



**Citation:** Yu, Y.; Zhang, J.; Lin, Y.; Zhao, D.; Li, Z.; Yan, S. Facile Synthesis of $Ni^{3+}/Co^{3+}$ Ion-Doped $Zn_2SnO_4$ Microspheres toward Efficient Photocatalytic $CO_2$ Reduction. *Appl. Sci.* **2023**, *13*, 13193. https://doi.org/10.3390/app132413193

Academic Editors: Lifang Chen, Luis Enrique Noreña and Jin An Wang

Received: 17 November 2023
Revised: 7 December 2023
Accepted: 10 December 2023
Published: 12 December 2023



## 1. Introduction

The excessive emission of $CO_2$ has caused great harm to the environment and human beings. $CO_2$ is the main greenhouse gas that causes global warming, which has brought about a series of environmental problems, including melting ice caps and glaciers, rising sea levels, changes in precipitation patterns, more extreme weather events, and biodiversity loss [1,2]. The increase in $CO_2$ concentration in the atmosphere has also led to a decrease in the pH value of the ocean, resulting in ocean acidification. This has damaged marine ecosystems and the ability of coral reefs to survive, affecting fisheries and other industries that rely on ocean resources. Moreover, human health is also affected by high concentrations of $CO_2$ in the atmosphere. Exposure to high concentrations of $CO_2$ can cause respiratory problems, such as asthma and other respiratory infections. To address the issue of excessive $CO_2$ emissions, it is necessary to take measures to reduce emissions. This includes using clean energy sources, such as solar, wind, and nuclear energy, instead of coal and other fossil fuels that emit large amounts of $CO_2$ [3]. In addition, planting trees and other carbon-absorbing plants can help absorb some of the excess $CO_2$ in the atmosphere. Finally, policies should be implemented to encourage more sustainable practices and reduce emissions from vehicles and other sources. The burning of fossil fuels, such as coal, oil, and natural gas has produced a large amount of greenhouse gas emission, especially $CO_2$, which has caused global climate change and environmental problems [4,5]. To solve these serious problems, developing clean and renewable energy sources, such as solar energy, is of great importance for human beings [6]. As a new type of technology, the photocatalytic reduction of $CO_2$ into hydrocarbons has drawn a lot of attention, as it converts the greenhouse gas, $CO_2$, into renewable energy via solar light irradiation, solving the energy crisis and greenhouse effect simultaneously [7–9].

One of the most commonly used photocatalysts for $CO_2$ reduction is titanium dioxide ($TiO_2$), which has a high photocatalytic activity and stability under UV light. The photocatalytic reduction process typically involves two main steps: (1) the absorption of light by

the photocatalyst, resulting in the generation of electron–hole pairs, and (2) the transfer of the electrons to a reducing agent, such as $H_2$ or CO, to generate the desired product. In the first step, the photocatalyst absorbs light energy, typically in the form of visible or ultraviolet light, and generates excited electrons. These electrons are transferred to the surface of the photocatalyst, where they can participate in reduction reactions. The excited electrons reduce the $CO_2$ molecule, which is adsorbed on the photocatalyst surface. This reduction process involves the addition of electrons to the $CO_2$ molecule, reducing it to a lower-energy species. One common product of this reduction process is methane ($CH_4$), but other compounds such as methanol or formic acid can also be produced. The overall process of photocatalytic reduction of $CO_2$ involves several steps, including the absorption of light by the photocatalyst, the generation of excited electrons, the reduction of $CO_2$, and the formation of the final product. The mechanism is highly efficient and can convert $CO_2$ into useful compounds without the need for external reducing agents. This process has attracted significant interest for its potential to convert waste $CO_2$ into valuable products while reducing the environmental impact of industrial processes.

The main advantage of photocatalytic reduction is that it can convert $CO_2$ into useful chemicals without the need for high temperatures or pressures. In addition, photocatalytic reduction can be achieved using solar energy, making it a sustainable and environmentally friendly process. However, there are still some challenges in implementing photocatalytic reduction on a large scale. These include improving the quantum efficiency of the process, increasing the selectivity for the desired product, and reducing the cost of the catalyst [4,5,9]. Future research efforts will focus on overcoming these challenges to make photocatalytic reduction a more practical and efficient method for converting $CO_2$ into useful chemicals.

During the last decades, various semiconductors have been investigated as potential candidate photocatalysts for efficient and practical $CO_2$ reduction, such as $TiO_2$ [6], $ZnGa_2O_4$ [4], $LaPO_4$ [9], $WO_3$ [10], ZnS [11,12], and bismuthates [13,14]. As one of the most investigated photocatalysts, $TiO_2$ has a wide range of applications, including environmental pollution control, energy conversion, and organic wastewater treatment. The photocatalytic activity of $TiO_2$ is based on its ability to absorb ultraviolet light and generate electron–hole pairs, which are responsible for the activation of oxygen and the reduction of electron acceptors. The holes generated in the valence band of $TiO_2$ can react with water to produce hydroxyl radicals (•OH), while the electrons in the conduction band can reduce the adsorbed species on the catalyst surface. $TiO_2$ photocatalysis has been widely used for environmental purification, including the decomposition of organic pollutants in air and water. In addition, $TiO_2$ photocatalysis can also be used for energy conversion, such as in solar cells and artificial photosynthesis, to convert solar energy into chemical energy. The performance of $TiO_2$ photocatalysts is influenced by factors such as crystal structure, particle size, and surface structure. Nanostructured $TiO_2$ with a smaller particle size has a higher specific surface area and more active sites, resulting in higher photocatalytic activity. In addition, the surface structure and morphology of the catalyst can also affect its performance by providing more active sites or faster electron transfer kinetics. Despite its wide range of applications, $TiO_2$ photocatalysis still faces challenges such as its low activity in the visible light region and its sensitivity to water quality and environmental conditions [6,15,16]. Future research should focus on overcoming these limitations to further improve the efficiency and practicality of $TiO_2$ photocatalysis in various applications.

Up to now, many efforts have been devoted to improving the photocatalytic activity of semiconductors on $CO_2$ reduction, such as doping or modification with foreign elements, composition with other semiconductors, and the adjustment of nanostructures [11,17–19]. However, most of these photocatalysts exhibit poor photocatalytic performance for practical application, because of the large band gap and the rapid recombination of charge carriers [20,21]. It is still necessary to further improve photocatalytic performance by developing a new type of photocatalyst with strong redox ability, a visible response, and high photocatalytic performance.

$Zn_2SnO_4$, also known as ZTO, is a ternary oxide semiconductor material with a cubic crystal structure in which zinc and tin exist in a tetrahedral coordination form and oxygen exists in a bidentate coordination form. The band gap of $Zn_2SnO_4$ material at room temperature is about 3.6 eV, which has good insulating properties and chemical stability. In addition, $Zn_2SnO_4$ also has high electrical conductivity, fast electron transfer, high chemical sensitivity, and excellent visible light absorption. $Zn_2SnO_4$ has wide application value in many fields. $Zn_2SnO_4$ is a versatile material with potential for a wide range of applications. Its unique physical and chemical properties make it widely applicable in energy, environmental monitoring, and fire prevention. With the continuous advancement of science and technology, the application areas of $Zn_2SnO_4$ will continue to expand, bringing more contributions to the development of human society [18,22–24].

$Zn_2SnO_4$ has been widely investigated as a photocatalyst, owing to its high electric conductivity, high electron mobility, stability, and charming optical properties [18,22–24]. Wang et al. composited ZTO with $SnO_x$ by a one-pot hydrothermal method [23]. The composited photocatalysts exhibit improved photocatalytic performance for the degradation of methyl orange (MO) and gaseous benzene. Shi and Dai synthesized highly ordered $Zn_2SnO_4$ nanotube arrays by using ZnO arrays as templates [25]. These ZTO arrays exhibit enhanced photocatalytic activity. Julio et al. synthesized high crystalline $Zn_2SnO_4$ nanostructures using a hydrothermal method [26]. They modified the $Zn_2SnO_4$ nanostructure with Pt to improve the photocatalytic performance of $H_2$ production. Ren et al. synthesized $Zn_2SnO_4$ with Mo doping and oxygen vacancies with high photocatalytic activity on HCHO oxidation [27]. Mo doping and the introduction of oxygen vacancies would extend the visible response, promote the separation of charge carriers, and induce new reactive sites for the ZTO-based photocatalysts. Hong et al. composited ZTO with ZIF-8, which exhibits significant photocatalytic performance on Methylene Blue (MB) degradation [22]. Our previous work also reported a simple synthesis of $Sn^{4+}$ ions self-doped $Zn_2SnO_4$ nanoplates [18]. The $Sn^{4+}$ ions would induce a new doping energy level below the conduction band of ZTO. The visible response is extended, and charge carriers are separated. As a result, the photocatalytic activity on the $CO_2$ reduction of $Sn^{4+}$ ions self-doped $Zn_2SnO_4$ nanoplates is significantly improved. However, the detailed influence of the doped elements on the band structure and photocatalytic performance of ZTO-based photocatalysts still needs further investigation.

In this work, Co and Ni, two iron family elements, were selected to be weaved into the lattice of $Zn_2SnO_4$ to investigate the influence of foreign elements on the band structure and photocatalytic performance of $Zn_2SnO_4$ samples. The photocatalytic reduction of $CO_2$ into $CH_4$ was applied to evaluate the photocatalytic performance of the as-prepared catalysts. It was revealed that the lattice $Zn^{2+}$ ions were replaced by the $Co^{3+}$ or $Ni^{3+}$ ions in the substitutional mode. The doped $Co^{3+}$ or $Ni^{3+}$ ions would induce a new doping energy level in the band gap of $Zn_2SnO_4$. As a result, the light response is enhanced, the charge carriers are separated, and the photocatalytic activity is improved for the Ni-doped $Zn_2SnO_4$ and Co-doped $Zn_2SnO_4$ samples. The photocatalytic mechanism of the enhanced $CO_2$ reduction is also discussed.

## 2. Experimental Details

### *2.1. Preparation of Photocatalysts*

All the chemicals used in this work were of analytical grade and without any further purification. At room temperature (25 °C), 1.066 g of $Na_2SnO_3{\cdot}3H_2O$ and 1.09 g of $ZnCl_2$ were dissolved in the mixture of 38 mL deionized water and 2 mL of NaOH solution (1 mol/L) under vigorous stirring for 40 min. Then, 5 mg of $NiCl_2{\cdot}6H_2O$ or $CoCl_2{\cdot}6H_2O$ was added into the suspension under vigorous stirring for 40 min. Then, the whole suspension was transferred to a 50 mL Teflon-lined autoclave and heated at 200 °C for 24 h. After naturally cooling down to room temperature, the obtained precipitate was washed with ethanol and deionized water six times. The obtained precipitate was centrifuged and dried in an oven at 60 °C for 24 h. The obtained powders were designated as Ni-ZTO

or Co-ZTO. In addition, the pure $Zn_2SnO_4$ samples were synthesized by removing the corresponding precursors and designated as ZTO.

### 2.2. Characterization

Powder X-ray diffraction (XRD) studies were carried out on a Japan Rigaku Smartlab SE; the scanning range is from 10° to 80°, and the scanning speed is 10°/min. The XPS was carried out by the Scientific ESCALAB 250Xi. The excitation source is Al Kα rays (1486.6 eV). The gas chromatograph is GC2010 PLUS, Shimadzu, Japan. The samples' morphologies were analyzed through a JSM-7800F scanning electron microscope (SEM). Using a JEM-2800 microscope, the high-resolution TEM (HRTEM) images were tested. The UV-vis measurement of the samples was carried out by a spectrophotometer with Shimadzu UV-3600i Plus. The electrochemical measurements were performed in a previous report [28].

### 2.3. Photocatalytic Reduction of Carbon Dioxide

The photocatalytic reaction to convert carbon dioxide into methane was conducted in a sealed 275 mL Pyrex glass reactor. A total of 100 mg of the as-prepared samples were uniformly dispersed on the rounded base of the Pyrex glass reactor, which had an area of approximately 18 $cm^2$. The Pyrex glass reactor was then inflated with $CO_2$ gas (99.999%) at a flux of 300 mL/min for 45 min to exclude air (e.g., $O_2$ and $N_2$). Subsequently, 400 mg of deionized water was injected into the Pyrex glass reactor, which was then sealed. The Pyrex glass reactor was positioned 25 cm directly beneath a 500 W Xe lamp. Every 2 h, 0.4 mL of gas was extracted to determine the yield of CO and $CH_4$ using a gas chromatograph (GC 2010 plus, Shimadzu, Japan) modified with a FID detector, a packed column, and a converter loaded with Ni catalysts. A certain amount (0.4 mL) of CO and $CH_4$ gas, with calibrated concentrations, was initially detected using a gas chromatograph to measure the peak area associated with CO and $CH_4$. Consequently, the concentrations of the resulting CO and CH4 gas can be determined based on the respective peak areas. The quantity of CO and CH4 produced can be calculated by multiplying the volume of the reactor.

## 3. Results and Discussion

To investigate the crystal structure of the ZTO-based samples, the XRD patterns of ZTO, Co-ZTO, and Ni-ZTO are shown in Figure 1A. All three samples show strong and sharp XRD peaks at 2θ = 17.7°, 29.1°, 34.3°, 35.9°, 41.7°, 51.7°, 55.1°, and 66.4°, corresponding to the (111), (220), (311), (222), (400), (422), (511), and (440) planes of $Zn_2SnO_4$ (JCPDS. No. 24-1470). There is no other diffraction peak related to $SnO_2$, ZnO, NiO, or CoO observed in Figure 1A. Figure 1B shows the enlargement of the (311) plane for ZTO, Ni-ZTO, and Co-ZTO around 34.3°. Compared with the pure ZTO samples, the peak position of the (311) plane for Co-ZTO and Ni-ZTO shifted to a larger diffraction angle. In addition, the lattice parameters and cell volume also decreased for Co-ZTO and Ni-ZTO, in comparison with the pure ZTO samples. This implies that the introduced Co and Ni atoms were weaved into the lattice of $Zn_2SnO_4$.

It is known that the ionic radius of $Zn^{2+}$ ions and $Sn^{4+}$ ions is 74 pm and 71 pm, respectively. As iron family elements, the valence of Co and Ni atoms usually exist as +2 or +3 in metal oxide. The ionic radius of $Co^{2+}$ and $Ni^{2+}$ is 74 pm and 72 pm. The ionic radius of $Co^{3+}$ and $Ni^{3+}$ is 63 pm and 62 pm. According to the doping theory for metal oxide, it is difficult for the Ni and Co atoms to be incorporated into the $Zn_2SnO_4$'s lattice in the interstitial mode, as the ionic radius of Ni and Co is close to the ionic radius of Zn and Sn. Thus, it becomes reasonable to deduce that the Co and Ni ions are doped in the $Zn_2SnO_4$'s lattice in the substitutional mode. Moreover, if the lattice's $Zn^{2+}$ or $Sn^{4+}$ ions are replaced by $Co^{2+}$ or $Ni^{2+}$ ions, the lattice parameters and cell volume of $Zn_2SnO_4$ should remain unchanged, owing to the similar ionic radius. If the lattice's $Zn^{2+}$ or $Sn^{4+}$ ions are replaced by $Co^{3+}$ or $Ni^{3+}$ ions, the lattice parameters and cell volume of $Zn_2SnO_4$ should be reduced, as the ionic radius of the $Co^{3+}$ ions (63 pm) and $Ni^{3+}$ ions (62 pm) is much smaller than

that of the $Zn^{2+}$ ions (74 pm) and $Sn^{4+}$ ions (71 pm). According to experimental data in Figure 1B and Table 1, it is reasonable to deduce that the $Co^{3+}$ and $Ni^{3+}$ ions are doped in the $Zn_2SnO_4$'s lattice in the substitutional mode. To further investigate the chemical states of the $Co^{3+}$ and $Ni^{3+}$ ions in $Zn_2SnO_4$, the XPS characterization is applied in the following section.

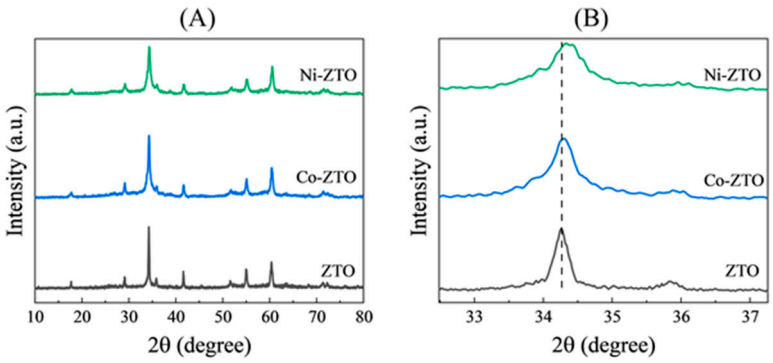


**Figure 1.** (**A**) XRD patterns of ZTO, Ni-ZTO, and Co-ZTO. (**B**) Enlarged XRD peaks of the (311) plane for ZTO, Ni-ZTO, and Co-ZTO.

**Table 1.** Lattice parameters and cell volume of pure ZTO, Co-ZTO, and Ni-ZTO samples.

| Sample | Lattice Parameters | | | Cell Volume (Å$^3$) |
|---|---|---|---|---|
| | a | b | c | |
| ZTO | 8.6711 | 8.6711 | 8.6711 | 651.97 |
| Co-ZTO | 8.6546 | 8.6546 | 8.6546 | 648.24 |
| Ni-ZTO | 8.6414 | 8.6414 | 8.6414 | 645.29 |

As the existing states of the Co and Ni ions in $Zn_2SnO_4$ are closely related to the valence of the Co and Ni ions, the XPS Survey, Co 2p of the Co-ZTO sample, Ni 2p of the Ni-ZTO sample, O 1s, Zn 2p, and Sn 3d spectra for the ZTO, Co-ZTO, and Ni-ZTO samples are plotted in Figure 2. All the ZTO-based photocatalysts exhibit strong XPS peaks related to the C 1s, O 1s, Sn 3d, and Zn 2p. As shown in Figure 2B, a weak XPS peak centered at about 779.2 eV is observed for the Co-ZTO samples. This weak Co 2p peak can be ascribed to the $Co^{3+}$ ions [29]. As shown in Figure 2C, the weak XPS Ni 2p peak at about 855.6 eV can be attributed to the $Ni^{3+}$ ions [30]. Hence, it can be confirmed by the XPS that the introduced Co and Ni atoms exist as +3 valence in this work. Moreover, as the ionic radius of the $Co^{3+}$ ions (63 pm) and $Ni^{3+}$ ions (62 pm) is much smaller than that of $Zn^{2+}$ ions (74 pm) and $Sn^{4+}$ ions (71 pm), the lattice's $Zn^{2+}$ or $Sn^{4+}$ ions are replaced by $Co^{3+}$ or $Ni^{3+}$ ions in the substitutional mode, leading to the reduced parameters and cell volume. In Figure 2D, the lattice's O 1s peak is at about 530.1 eV, and the surface's O 1s peak is at about 531.5 eV for all three samples. In Figure 2E, the Zn $2p_{3/2}$ is at 1020.8 eV for ZTO and 1020.9 eV for Co-ZTO and Ni-ZTO. In Figure 2F, the Sn $3d_{5/2}$ and Sn $3d_{3/2}$ are at 486.2 eV and 494.7 eV for all ZTO-based samples.

To investigate the morphology of Co-doped $Zn_2SnO_4$ and Ni-doped $Zn_2SnO_4$, the TEM and HR-TEM images of Co-ZTO and Ni-ZTO are shown in Figure 3. As shown in Figure 3A,B, both the Ni-ZTO and Co-ZTO samples consist of microspheres with an average diameter of 300 nm~500 nm. Moreover, these microspheres are constructed by a series of nanoplates, which are intercrossed with each other by self-assembly. These microsphere structures may leave many pores on the surface, increase the specific surface area, and improve the stability of photocatalysts, eventually benefiting the photocatalytic performance. Moreover, as shown in Figure 3C, the fringe lattice spacing for Co-ZTO is estimated to be 0.488 nm, corresponding to the (111) plane of $Zn_2SnO_4$. As shown in Figure 3D, the lattice spacing for Ni-ZTO is estimated to be 0.260 nm, corresponding to the

(311) plane of $Zn_2SnO_4$. It should be noted that the lattice spacing for Co-ZTO and Ni-ZTO in the HR-TEM images is smaller than that of the standard $Zn_2SnO_4$ cards. This may be caused by the substitutionally doped $Co^{3+}$ and $Ni^{3+}$ ions in the $Zn_2SnO_4$'s lattice. Thus, it can be concluded from the TEM images that both the Co-ZTO and Ni-ZTO samples are composed of microspheres, which consist of nanoplates intercrossed with each other.

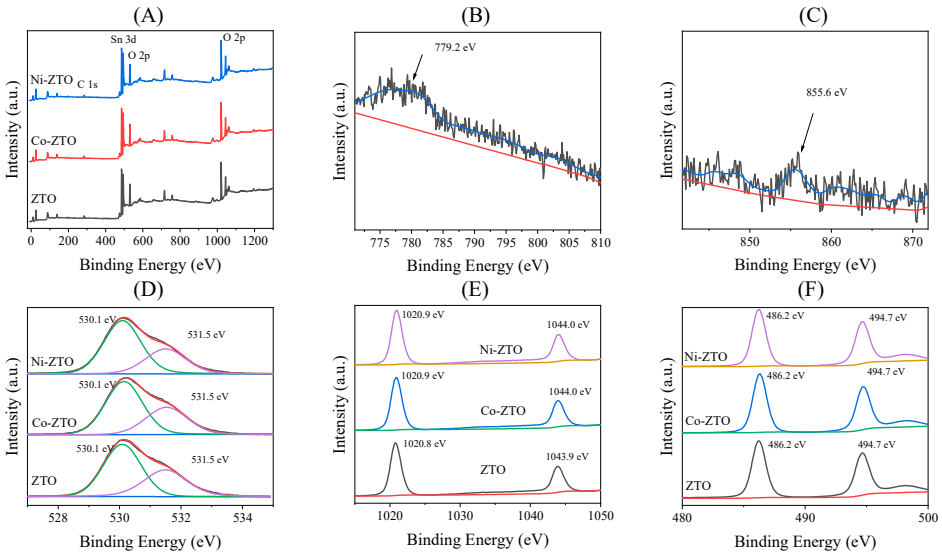


**Figure 2.** XPS (**A**) Survey, (**B**) Co 2p of the Co-ZTO sample, (**C**) Ni 2p of the Ni-ZTO sample, (**D**) O 1s, (**E**) Zn 2p, and (**F**) Sn 3d spectra for ZTO, Co-ZTO, and Ni-ZTO samples.

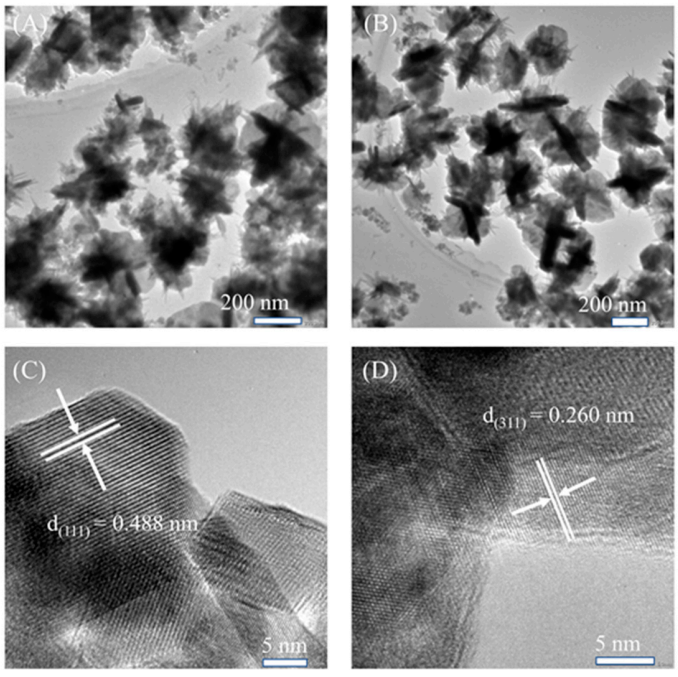


**Figure 3.** TEM image of (**A**) Co-ZTO and (**B**) Ni-ZTO; HR-TEM image of (**C**) Co-ZTO and (**D**) Ni-ZTO.

To better investigate the morphology of the as-prepared Co-ZTO and Ni-ZTO samples, the EDS elemental mapping of the Zn, Sn, O, Co and Zn, Sn, O, Ni for Co-ZTO, and Ni-ZTO samples are shown in Figures 4 and 5, respectively. It is clear in Figures 4 and 5 that the ZTO-based samples mainly consist of Zn, Sn, and O elements. In addition, a small amount of Ni and Co elements are randomly dispersed and did not enrich in some points. This also suggests the existence of $Co^{3+}$ and $Ni^{3+}$ ions doped in the lattice of $Zn_2SnO_4$ in the substitutional mode.

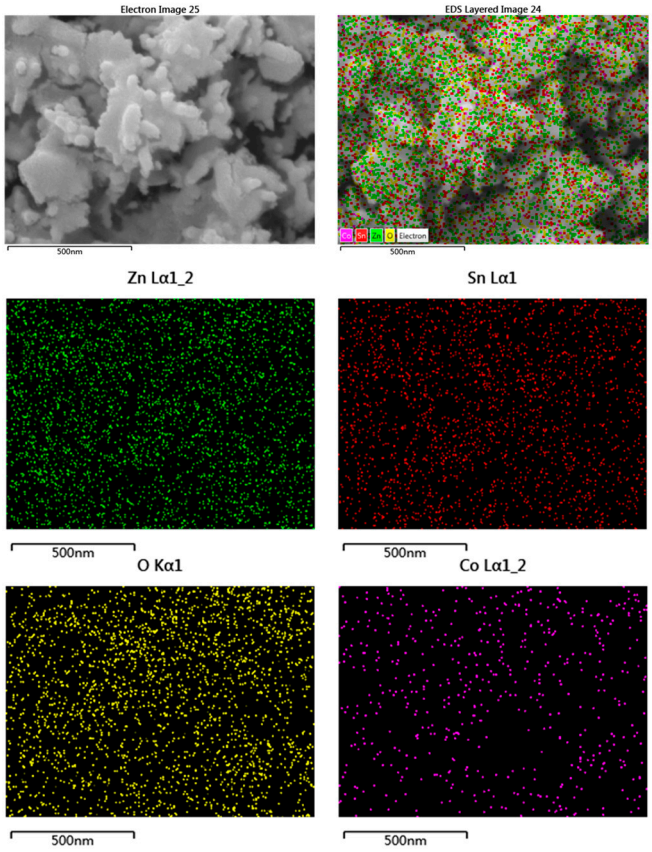


**Figure 4.** EDS elemental mapping of the Co-ZTO samples.

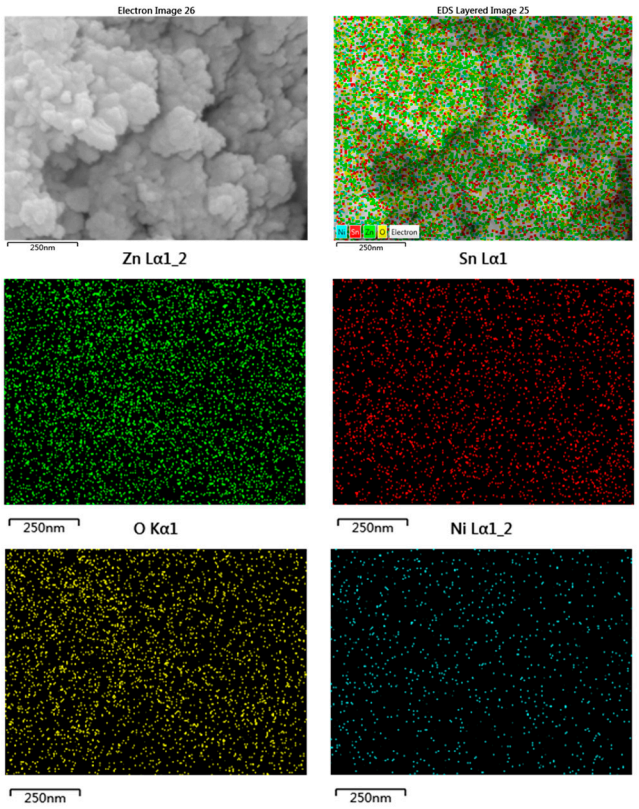


**Figure 5.** EDS elemental mapping of the Ni-ZTO samples.

To obtain physical insight into the band structure of $Co^{3+}$-doped $Zn_2SnO_4$ and $Ni^{3+}$-doped $Zn_2SnO_4$, a theoretical calculation based on the density functional theory calculation (DFT) is carried out, and the corresponding density of the states for ZTO, Co-ZTO, and Ni-ZTO is shown in Figure 6. Theoretical calculations were performed using the Vienna ab initio software package (VASP.5.4.4). As shown in Figure 6A, the band gap of pure ZTO is estimated to be about 0.93 eV, which is much smaller than the experimental data. This is because the DFT calculation usually underestimates the band gap of the semiconductors [31–33]. As shown in Figure 6B,C, the valence bands of Co-ZTO and Ni-ZTO are mainly composed of the O 2p states as well as the Sn and Zn states. The conduction bands of Co-ZTO and Ni-ZTO are mainly contributed by the Zn and Sn states, with a small amount of the O 2p states. Moreover, compared with pure ZTO samples, new doping energy levels occurred in the band gaps of Co-ZTO and Ni-ZTO, respectively. The introduced doping energy levels are mainly contributed by the Co/Ni and O elements, suggesting the occurred energy levels originated from the doped Co and Ni ions. Hence, it can be concluded that the introduced $Co^{3+}$ and $Ni^{3+}$ ions in the substitutional mode would induce new doping energy levels above the valence band of ZTO.

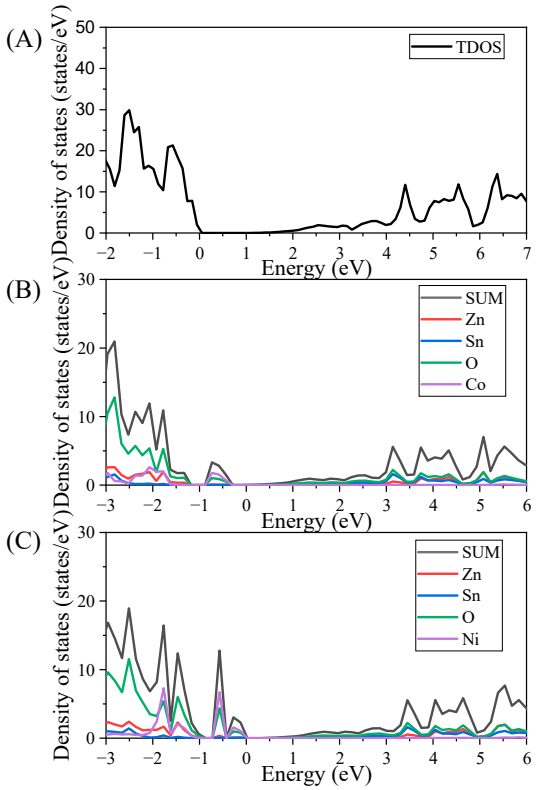


**Figure 6.** Calculated density of states (DOS) for the (**A**) ZTO, (**B**) Co-ZTO, and (**C**) Ni-ZTO samples.

To explore the influence of the doped Co and Ni ions on the band structure and light absorption capacity of the $Zn_2SnO_4$ samples, the UV-vis diffuse reflectance absorption spectra of the pure ZTO, Co-ZTO, and Ni-ZTO samples are shown in Figure 7A. The pure ZTO samples show strong absorption in the UV region, which can be attributed to the electrons' transition from the valence band to the conduction band of ZTO. For the Co-ZTO and Ni-ZTO samples, no blue shift or red shift is observed for the absorption edge of the spectra. This suggests that the doped $Co^{3+}$ and $Ni^{3+}$ ions did not change the band gap of the $Zn_2SnO_4$ microspheres. Moreover, it is found that the absorption spectra from the UV to the visible region are enhanced, which is caused by the doped $Co^{3+}$ and $Ni^{3+}$ ions in the substitutional mode. According to the DFT calculation results, the extended absorption can be ascribed to the electrons' transition from the energy levels of doped $Co^{3+}$ and $Ni^{3+}$ ions in the substitutional mode to the conduction band of ZTO. In addition,

the Tauc plots of ZTO, Co-ZTO, and Ni-ZTO are plotted in Figure 7B. The band gap for ZTO, Co-ZTO, and Ni-ZTO is estimated to be 3.30 eV. As the doped Co and Ni ions did not change the morphology and nanostructure of the ZTO microspheres, the band gap of Co-ZTO and Ni-ZTO remained unchanged, in comparison with the pure ZTO samples. Therefore, according to the UV-vis absorption spectra, it can be confirmed that new doping energy levels originated from the doped $Co^{3+}$ and $Ni^{3+}$ ions that occurred in the band gap of ZTO.

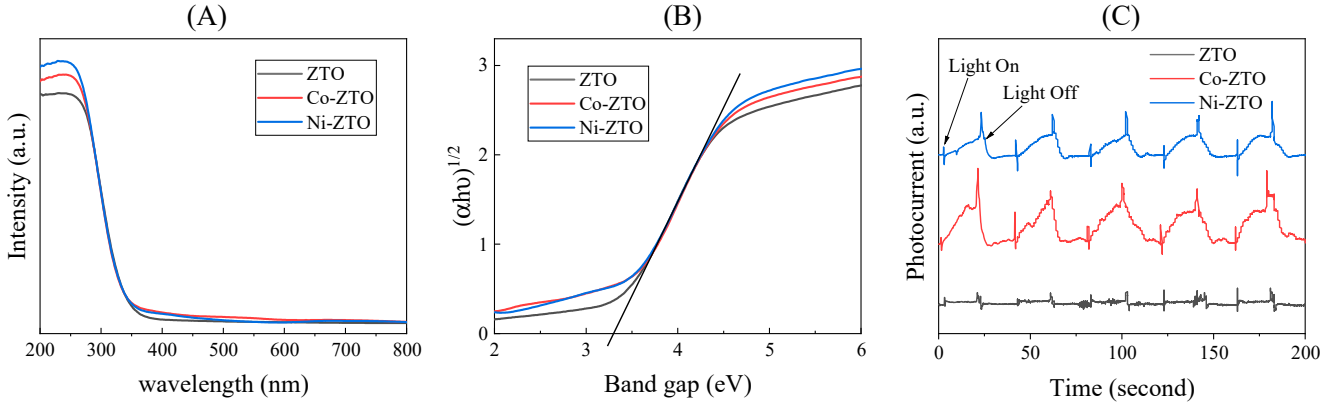


**Figure 7.** (**A**) UV-vis diffuse reflectance absorption spectra of the pure ZTO, Co-ZTO, and Ni-ZTO samples; (**B**) plots of $(ahv)^{1/2}$ versus photon energy for the pure ZTO, Co-ZTO, and Ni-ZTO samples; (**C**) photocurrent response versus time for the pure ZTO, Co-ZTO, and Ni-ZTO samples.

The efficient separation and transfer of photogenerated charge carriers is beneficial for enhancing photocatalytic performance. Figure 7C illustrates the photocurrent response versus time for the ZTO-based samples, which was analyzed to evaluate the separation efficiency of the charge carriers. Notably, the photocurrent response, as observed in Figure 7C, exhibited a remarkable improvement for Co-ZTO and Ni-ZTO when compared to pure ZTO, during five on/off repetition cycles of the light. This observation strongly indicates an enhanced separation efficiency of the charge carriers in the Co-ZTO and Ni-ZTO samples.

The photocatalytic reduction of $CO_2$ into $CH_4$ is performed to investigate the effect of doped $Co^{3+}$ and $Ni^{3+}$ ions on ZTO samples, shown in Figure 8. For the pure ZTO samples, only a small amount of $CH_4$ ($1.02 \times 10^{-7}$ mol) is yielded after 8 h irradiation. For the Co-ZTO samples, more $CH_4$ is produced under irradiation. There is about $1.78 \times 10^{-7}$ mol of $CH_4$ detected for 8 hours' irradiation. The Ni-ZTO samples exhibit the highest photocatalytic activity and about $1.92 \times 10^{-7}$ mol of $CH_4$ is produced, which is almost twice that for pure ZTO. Hence, doping Co or Ni ions into the lattice of ZTO is an effective method to improve the photocatalytic performance of ZTO-based photocatalysts.

Based on the experimental data and theoretical calculation results, the photocatalytic mechanism of ZTO, Co-ZTO, and Ni-ZTO can be explained as follows: under irradiation, only a small number of electrons can be excited from the valence band to the conduction band of ZTO. Hence, the pure ZTO samples exhibit poor photocatalytic activity in the $CO_2$ reduction. After the introduction of Co and Ni ions in the substitutional mode, new doping energy levels occurred above the valence band of ZTO, and the light response from the UV to the visible region was also enhanced. More electrons can be excited from the doping energy levels of Co or Ni ions to the conduction band of ZTO and take part in the photocatalytic reaction. The introduction of $Co^{3+}$ or $Ni^{3+}$ ions would also benefit the separation of the charge carriers. The holes would react with $H_2O$ to yield $H^+$. The electrons would react with $CO_2$ to generate CO as the immediate product, which would further react with $H^+$ and electrons to generate $CH_4$ as the final product. As a result, more $CH_4$ molecules would be produced for the Co-ZTO and Ni-ZTO samples. It is expected

that the photocatalytic activity can be further improved by optimizing the amount of doped Co and Ni ions.

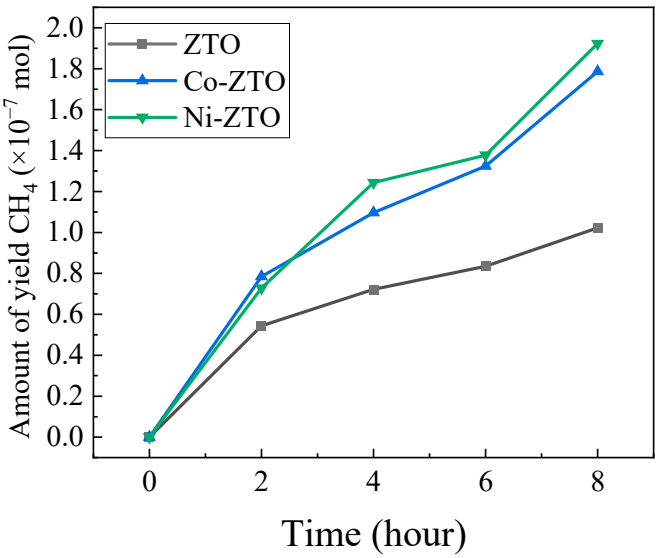


**Figure 8.** Photocatalytic activity on photocatalytic $CO_2$ reduction into $CH_4$ for the pure ZTO, Co-ZTO, and Ni-ZTO samples.

## 4. Conclusions

In this study, the researchers aimed to enhance the photocatalytic activity of ZTO ($Zn_2SnO_4$) microspheres by doping with $Co^{3+}$ and $Ni^{3+}$ ions. To achieve this, a hydrothermal method was employed for the preparation of doped ZTO microspheres. The photocatalytic activity of the $Co^{3+}$ and $Ni^{3+}$ ion-doped ZTO microspheres was found to be significantly improved compared to undoped ZTO. This improvement was observed specifically in the reduction of $CO_2$ into $CH_4$, indicating the potential of these doped microspheres for efficient $CO_2$ reduction. The doped $Co^{3+}$ and $Ni^{3+}$ ions were weaved in the lattice of ZTO in a substitutional mode. This substitution led to the creation of new energy levels above the valence band of ZTO, resulting in an improved separation efficiency of the carriers and enhanced photocatalytic activity. The findings of this study provide valuable insights into the physical mechanisms underlying the improved photocatalytic performance of ZTO-based photocatalysts for $CO_2$ reduction. By understanding the role of doping with $Co^{3+}$ and $Ni^{3+}$ ions, this work can help optimize the design and synthesis of ZTO-based materials for efficient $CO_2$ conversion.

**Author Contributions:** Conceptualization, D.Z.; Methodology, S.Y.; Software, D.Z.; Investigation, Z.L.; Resources, J.Z., Y.L. and Z.L.; Writing—original draft, Y.Y.; Writing—review & editing, S.Y.; Supervision, S.Y. All authors have read and agreed to the published version of the manuscript.

**Funding:** This work was supported by the National Natural Science Foundation of China under Grant No. 21805190, the Natural Science Foundation of the Jiangsu Higher Education Institutions of China under Grant No. 23KJB150004, and Natural Science Foundation of Huaiyin Institute of Technology under Grant No. 22HGZ011.

**Institutional Review Board Statement:** Not applicable.

**Informed Consent Statement:** Not applicable.

**Data Availability Statement:** Data are contained within the article.

**Conflicts of Interest:** The authors declare no conflict of interest.

## References


1. Zhu, Z.; Guo, W.; Zhang, Y.; Pan, C.; Xu, J.; Zhu, Y.; Lou, Y. Research progress on methane conversion coupling photocatalysis and thermocatalysis. *Carbon Energy* **2021**, *3*, 519–540. [CrossRef]
2. Jia, G.; Wang, Z.; Gong, M.; Wang, Y.; Li, L.H.; Dong, Y.; Liu, L.; Zhang, L.; Zhao, J.; Zheng, W.; et al. Ultrathin origami accordion-like structure of vacancy-rich graphitized carbon nitride for enhancing $CO_2$ photoreduction. *Carbon Energy* **2023**, *5*, e270. [CrossRef]
3. Wang, C.; Huang, H.; Weng, B.; Verhaeghe, D.; Keshavarz, M.; Jin, H.; Liu, B.; Xie, H.; Ding, Y.; Gao, Y.; et al. Planar heterojunction boosts solar-driven photocatalytic performance and stability of halide perovskite solar photocatalyst cell. *Appl. Catal. B Environ.* **2022**, *301*, 120760. [CrossRef]
4. Shi, Z.; Shi, D.; Zhang, L.; Cao, Y. Regulating the band structure by modifying $Ti_3C_2$ and doping Fe ions improved photocatalytic activity and selectivity of $ZnGa_2O_4$–$Ti_3C_2$–Fe for photoreducted $CO_2$ into $CH_4$. *J. Power Sources* **2022**, *535*, 231421. [CrossRef]
5. Shi, Z.; Li, H.; Zhang, L.; Cao, Y. Improved photocatalytic activity of $LaFeO_3$ with doping $Mn^{3+}$ ions and modifying $Pd^{2+}$ ions for photoreduction of $CO_2$ into $CH_4$. *J. Power Sources* **2022**, *519*, 230738. [CrossRef]
6. Zhou, Y.; Zhang, Q.; Shi, X.; Song, Q.; Zhou, C.; Jiang, D. Photocatalytic reduction of $CO_2$ into $CH_4$ over Ru-doped $TiO_2$: Synergy of Ru and oxygen vacancies. *J. Colloid Interface Sci.* **2022**, *608*, 2809–2819. [CrossRef]
7. Shitong, H.; Bifang, L.; Lijuan, H.; Hailing, X.; Zhengxin, D.; Jinlin, L. Construction of $ZnIn_2S_4$-$CdIn_2S_4$ Microspheres for Efficient Photo-catalytic Reduction of $CO_2$ with Visible Light. *Chin. J. Struct. Chem.* **2022**, *41*, 2201007–2201013.
8. Ya, L.; Fangbo, Y.; Feng, W.; Shengjie, B.; Guiwei, H. Construction of Z-Scheme $In_2S_3$-$TiO_2$ for $CO_2$ Reduction under Concentrated Natural Sunlight. *Chin. J. Struct. Chem.* **2022**, *41*, 2201034–2201039.
9. Yan, S.; Chen, L.; Peng, F.; Fan, Y.; Yu, Y.; Liu, Y.; Cao, Y. Interface modification by defect engineering for g-$C_3N_4$/$LaPO_4$−x nanorods towards efficient $CO_2$ photoreduction. *New J. Chem.* **2022**, *46*, 18776–18786. [CrossRef]
10. Huang, S.; Long, Y.; Ruan, S.; Zeng, Y.-J. Enhanced Photocatalytic $CO_2$ Reduction in Defect-Engineered Z-Scheme $WO_3$–x/g-$C_3N_4$ Heterostructures. *ACS Omega* **2019**, *4*, 15593–15599. [CrossRef]
11. Zhao, Q.; Li, H.; Cao, Y. Effect of $In(OH)_3$ species modified ZnS on improved photocatalytic activity of photoreduction of $CO_2$. *J. Solid State Chem.* **2021**, *296*, 121976. [CrossRef]
12. Feng, W.; Lei, Y.; Wu, X.; Yuan, J.; Chen, J.; Xu, D.; Zhang, X.; Zhang, S.; Liu, P.; Zhang, L.; et al. Tuning the interfacial electronic structure via Au clusters for boosting photocatalytic $H_2$ evolution. *J. Mater. Chem. A* **2021**, *9*, 1759–1769. [CrossRef]
13. Shtarev, D.S.; Shtareva, A.V.; Kevorkyants, R.; Molokeev, M.S.; Serpone, N. Revisiting the $BaBiO_3$ semiconductor photocatalyst: Synthesis, characterization, electronic structure, and photocatalytic activity. *Photochem. Photobiol. Sci.* **2021**, *20*, 1147–1160. [CrossRef] [PubMed]
14. Shtarev, D.S.; Serpone, N. A new generation of visible-light-active photocatalysts—The alkaline earth metal bismuthates: Syntheses, compositions, structures, and properties. *J. Photochem. Photobiol. C Photochem. Rev.* **2022**, *50*, 100501. [CrossRef]
15. Kumar, A.; Singla, Y.; Sharma, M.; Bhardwaj, A.; Krishnan, V. Two dimensional S-scheme $Bi_2WO_6$–$TiO_2$–$Ti_3C_2$ nanocomposites for efficient degradation of organic pollutants under natural sunlight. *Chemosphere* **2022**, *308*, 136212. [CrossRef] [PubMed]
16. Yu, Y.; Jiang, P.; Yan, Y.; Li, H.; Zhang, L.; Jiang, S.; Yang, W.; Cao, Y. Animal heat activated cancer therapy by a traditional catalyst TiO2-Pd/graphene composites. *Sci. Rep.* **2020**, *10*, 15823. [CrossRef] [PubMed]
17. Li, H.; Zhang, L.; Cao, Y. Synthesis of palladium-modified MnS photocatalysts with enhanced photocatalytic activity in the photoreduction of $CO_2$ to $CH_4$. *Appl. Surf. Sci.* **2021**, *541*, 148519. [CrossRef]
18. Yan, S.; He, Z.; Zhou, G.; Yu, Y.; Cao, Y. Hexagonal $Zn_2SnO_4$ nanoplates self-doped with $Sn^{4+}$ ions towards efficient photoreduction of $CO_2$ into $CH_4$. *Mater. Sci. Semicond. Process.* **2021**, *130*, 105818. [CrossRef]
19. Li, J.; Huang, H.; Xue, W.; Sun, K.; Song, X.; Wu, C.; Nie, L.; Li, Y.; Liu, C.; Pan, Y.; et al. Self-adaptive dual-metal-site pairs in metal-organic frameworks for selective $CO_2$ photoreduction to $CH_4$. *Nat. Catal.* **2021**, *4*, 719–729. [CrossRef]
20. Ali, K.A.; Abdullah, A.Z.; Mohamed, A.R. Visible light responsive $TiO_2$ nanoparticles modified using Ce and La for photocatalytic reduction of $CO_2$: Effect of Ce dopant content. *Appl. Catal. A* **2017**, *537*, 111. [CrossRef]
21. Tahir, M. Synergistic effect in MMT-dispersed Au/$TiO_2$ monolithic nanocatalyst for plasmon-absorption and metallic interband transitions dynamic $CO_2$ photo-reduction to CO. *Appl. Catal. B Environ.* **2017**, *219*, 329–343. [CrossRef]
22. Hong, Y.; Wang, B.; Hu, S.; Lu, S.; Wu, Q.; Fu, M.; Gu, C.; Wang, Y. Preparation and photocatalytic performance of $Zn_2SnO_4$/ZIF-8 nanocomposite. *Ceram. Int.* **2023**, *49*, 11027–11037. [CrossRef]
23. Wang, J.; Li, H.; Meng, S.; Zhang, L.; Fu, X.; Chen, S. One-pot hydrothermal synthesis of highly efficient SnOx/$Zn_2SnO_4$ composite photocatalyst for the degradation of methyl orange and gaseous benzene. *Appl. Catal. B Environ.* **2017**, *200*, 19–30. [CrossRef]
24. Wang, H.-Y.; Wang, B.-Y.; Meng, J.-K.; Wang, J.-G.; Jiang, Q.-C. One-step synthesis of Co-doped $Zn_2SnO_4$–graphene–carbon nanocomposites with improved lithium storage performances. *J. Mater. Chem. A* **2015**, *3*, 1023–1030. [CrossRef]
25. Shi, L.; Dai, Y. Synthesis and photocatalytic activity of $Zn_2SnO_4$ nanotube arrays. *J. Mater. Chem. A* **2013**, *1*, 12981–12986. [CrossRef]
26. Núñez, J.; Fresno, F.; Collado, L.; Jana, P.; Coronado, J.M.; Serrano, D.P.; de la Peña O'Shea, V.A. Photocatalytic $H_2$ production from aqueous methanol solutions using metal-co-catalysed $Zn_2SnO_4$ nanostructures. *Appl. Catal. B Environ.* **2016**, *191*, 106–115. [CrossRef]
27. Ren, Z.; Chen, B.; Li, Y.; Carabineiro, S.A.C.; Duan, Y.; Dong, F. Remarkable formaldehyde photo-oxidation efficiency of $Zn_2SnO4$ co-modified by Mo doping and oxygen vacancies. *Sep. Purif. Technol.* **2023**, *310*, 123202. [CrossRef]

28. Yan, S.; Zhang, X.; Wu, D.; Yu, Y.; Ding, Z. A system investigation on Ru-MOF-74 with efficient photocatalytic nitrogen fixation performance. *Surf. Interfaces* **2022**, *33*, 102225. [CrossRef]
29. Li, K.; Chen, C.; Bian, X.; Sun, T.; Jia, J. Electrolytic nitrate reduction using $Co_3O_4$ rod-like and sheet-like cathodes with the control of (220) facet exposure and $Co^{2+}/Co^{3+}$ ratio. *Electrochim. Acta* **2020**, *362*, 137121. [CrossRef]
30. Fu, Z.; Hu, J.; Hu, W.; Yang, S.; Luo, Y. Quantitative analysis of $Ni^{2+}/Ni^{3+}$ in Li[NixMnyCoz]$O_2$ cathode materials: Non-linear least-squares fitting of XPS spectra. *Appl. Surf. Sci.* **2018**, *441*, 1048–1056. [CrossRef]
31. Huang, G.; Li, S.; Liu, L.; Zhu, L.; Wang, Q. $Ti_3C_2$ MXene-modified $Bi_2WO_6$ nanoplates for efficient photodegradation of volatile organic compounds. *Appl. Surf. Sci.* **2020**, *503*, 144183. [CrossRef]
32. Zhang, R.; Song, L.; Liu, H.; Wang, B. The interaction mechanism of $CO_2$ with $CH_3$ and H on Cu (111) surface in synthesis of acetic acid from $CH_4/CO_2$: A DFT study. *Appl. Catal. A* **2012**, *443–444*, 50–58. [CrossRef]
33. Finazzi, E.; Di Valentin, C.; Pacchioni, G. Boron-doped anatase $TiO_2$: Pure and hybrid DFT calculations. *J. Phys. Chem. C* **2008**, *113*, 220–228. [CrossRef]